RSC Advances

PAPER

View Article Online
View Journal | View Issue

Cite this: *RSC Adv.*, 2026, **16**, 3469

Molybdenum disulfide-grafted carbon nanotubes for the electrochemical detection of acetaminophen with ultra-sensitivity

Siying Fu,†[ab] Juan Li,†[c] Kunru Liu,[d] Huan Tao,[b] Wenyan Guo,[d] Qingbing Zha,*[ab] Jinhua Li*[be] and Zhi Li *[e]

The overuse of acetaminophen (APAP) poses significant health risks to human health, which necessitates the development of an efficient and rapid detection method for APAP. Hence, an electrochemical sensor using molybdenum disulfide-grafted carbon nanotubes (MoS_2/CNTs) was developed for the ultra-sensitive detection of acetaminophen (APAP). The linear detection range of the sensor was 0.07 to 150 μM, and the limit of detection for APAP was 0.43 μM. The MoS_2/CNTs composite demonstrated significantly enhanced catalytic activity toward APAP, attributed to its enormous specific surface area and effective electron transport characteristics. Electrochemical techniques, including impedance spectroscopy (EIS), cyclic voltammetry (CV), and differential pulse voltammetry (DPV), were further performed to assess the functionality of the sensor. Furthermore, the sensor exhibited high selectivity and excellent stability and reproducibility. Additionally, it was demonstrated to be effective for APAP detection across a range of authentic samples, including commercial tablets, tap water, and urine. The MoS_2/CNTs electrochemical sensor offers a sensitive, cost-effective solution for drug and biological small-molecule detection in environmental and medical fields.

Received 27th September 2025
Accepted 23rd December 2025

DOI: 10.1039/d5ra07347b

rsc.li/rsc-advances

1. Introduction

In recent decades, acetaminophen (APAP) has become a widely used antipyretic and analgesic that is essential in daily life.[1] However, its excessive intake causes nephrotoxicity and liver toxicity in humans.[2,3] For this reason, it is crucial to measure the amount of APAP in bodily fluids like blood, serum, and urine. Although numerous analytical techniques, including spectrophotometry, high-performance liquid chromatography (HPLC), and chemiluminescence, have been developed for APAP detection,[4–7] they suffer from limitations such as high costs and complex operational processes. Conversely, electrochemical sensing technologies have attracted a lot of interest due to their ease of use, exceptional selectivity, high sensitivity, rapid response times, extensive linear detection ranges, and straightforward sample preparation requirements.[8–10]

It is well established that the performance of electrochemical sensors is closely linked to the characteristics of the modified electrode materials. It has been reported that electrochemical performance can be enhanced by the use of rationally engineered nanomaterials, including reduced graphene oxide hybrids, metal oxide nanoparticles, and noble-metal decorated carbon frameworks.[11–15] Among these, carbon nanotubes (CNTs) stand out due to their one-dimensional tubular structure, large surface area, and high electrical conductivity,[16] which together facilitate efficient electron transport and accelerate redox kinetics at the electrode interface.[17] CNTs are regarded as ideal candidates for electrode modification because of their high electrical conductivity, mechanical strength, and biocompatibility.[18] Numerous nanocomposites have been developed by integrating CNTs to further enhance sensing performance, such as the NH_2-CNTs/ZnO and β-CD/CNTs composites reported by Balram *et al.*[19] and Alam *et al.*,[20] respectively.

Recently, layered transition-metal dichalcogenides (such as WS_2, MoS_2, SnS_2 and VS_2) have received increasing interest in the electrochemical field due to their high specific surface area and mass transfer effects. Molybdenum disulfide (MoS_2), consisting of two Mo layers positioned between sulfur layers *via* weak van der Waals forces, exhibits an asymmetric structure[21] and exceptional electrical transport capabilities owing to the two-dimensional electron–electron correlations among the Mo

[a]*Department of Clinical Laboratory Medicine, The Sixth Affiliated Hospital of Jinan University, Dongguan, 523000, PR China. E-mail: zhaqingbb@sina.com*

[b]*Department of Clinical Laboratory Medicine, Department of Ultrasound, The First Affiliated Hospital of Jinan University, Guangzhou, 510630, PR China. E-mail: lijinhua@jnu.edu.cn*

[c]*School of Stomatolgy, Jinan University, Guangzhou, 510632, PR China*

[d]*Department of Clinical Laboratory Medicine, General Hospital of Southern Theater Command PLA, Guangzhou, 510010, PR China*

[e]*Department of Ultrasound, Guangdong Provincial Key Laboratory of Spine and Spinal Cord Reconstruction, The Fifth Affiliated Hospital of Jinan University (Heyuan Shenhe People's Hospital), Heyuan, 517000, PR China. E-mail: zhili@jnu.edu.cn*

† These authors contributed equally to this work.

atoms.[22,23] Owing to its intrinsic layered structure, various atoms or molecules can be inserted into the interlayers through intercalation techniques.[24] However, the performance of MoS_2 is limited by certain structural and interfacial constraints, resulting in poor electrical conductivity and moderate cycling stability. To address these challenges, extensive research has focused on modifying the morphology, structure, and interfacial characteristics of MoS_2.[25] A particularly effective strategy involves constructing structured nanocomposites by integrating additional electroactive components. Moreover, synergies between carbon-based materials and metal or metal oxide nanoparticles in electrocatalytic applications have been empirically validated.[26] Consequently, the integration of CNTs with the layered MoS_2 structure is expected to yield a similar improvement in the performance of electrochemical sensors.

In this study, MoS_2 was synthesized *via* hydrothermal methods and subsequently combined with CNTs through a simple physical mixing technique to form a MoS_2/CNTs composite. The electrochemical sensor, which was created by depositing this combination over a glassy carbon electrode (GCE), demonstrated outstanding analytical performance in detecting APAP. Because of its huge specific surface area and effective electron transfer capacity, the sensor demonstrated a low limit of detection (LOD) and a wide linear detection range. It also exhibited good reproducibility and selectivity and could detect APAP in real samples such as pills, urine, and tap water. These results demonstrate the remarkable potential for environmental and life health monitoring.

2. Experimental section

Chemicals and characterization details can be found in SI (Text S1 and S2).

2.1 Synthesis of MoS_2 nanosheets

MoS_2 nanosheets were synthesized by using the standard hydrothermal method according to a previous report.[27] First, 1.236 g $(NH_4)_6Mo_7O_{24}\cdot 4H_2O$ (*ca.* 1 mmol) and 0.2283 g CH_4N_2S (*ca.* 3 mmol) were added to 60 mL of water and ultrasonicated for 1 h. The solution was then heated at 210 °C for 24 h in a 100 mL Teflon-lined autoclave. After cooling to room temperature, the material was collected and cleaned with water, then dispersed in 50 mL *N*-methyl formamide under ultrasonication for 1 h. The final steps involved separating the products by centrifugation and washing with ethanol and water three times. The obtained powders were dried in an oven at 60 °C overnight to give the MoS_2 nanosheets.

2.2 Fabrication of MoS_2/CNTs sensor

Firstly, the MoS_2 nanosheets were synthesized by the method described above. Secondly, 2 mg mL^{-1} of the complex solution

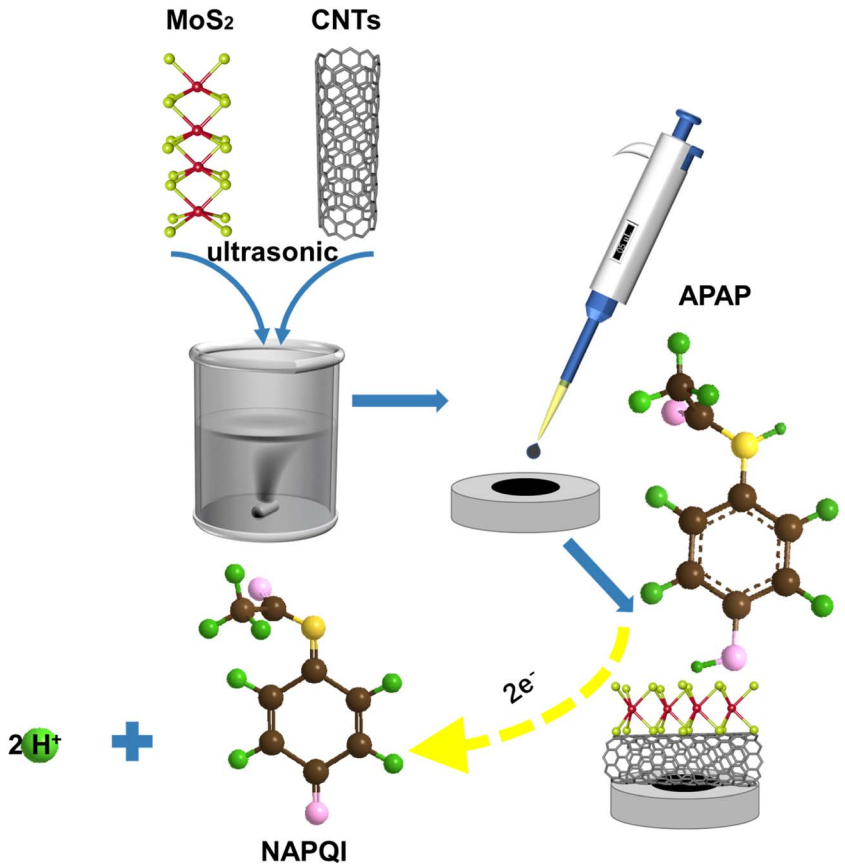

Scheme 1 Preparation process of the MoS_2/CNTs sensor.

was obtained by physically mixing CNTs with MoS_2 in different proportions (weight ratios of MoS_2 to CNTs were 3 : 1, 2 : 1, 1 : 1, 1 : 2 and 1 : 3) in an ethanol–water mixture ($V_{water}/V_{ethanol}$ = 1 : 1). Lastly, the dispersions were sonicated for 30 min. Before use, the GCE was thoroughly rinsed with deionized water and ethanol, polished with polishing paper and alumina powder, sonicated in deionized water and dried completely. Then, 5.0 μL of the solution of the MoS_2/CNTs composite was dropped on the GCE surface and dried (Scheme 1). For comparison, CNT and MoS_2 electrodes were prepared by the same method under the same conditions.

2.3 Apparatus

All electrochemical measurements were performed with a typical three-electrode system on the CHI 760 E electrochemical workstation. The standard three-electrode analysis system was adopted using a platinum electrode (counter electrode), a saturated calomel electrode (reference electrode), and MoS_2/CNTs modified GCE (working electrode). The electrochemical detection of APAP was performed using the differential pulse voltammetry (DPV) method. The parameters were as follows: the amplitude, pulse width, potential range and incremental potential were set as 50 mV, 0.05 s, 0 to 0.8 V and 0.004 V, respectively. The electrochemical performance of the constructed sensor was assessed with cyclic voltammetry (CV). The CV analysis parameters of scan rate, potential range, and sample interval were set as 100 mV s^{-1}, 0 to 0.8 V, and 0.001 V, respectively. Electrochemical impedance spectroscopy (EIS) was evaluated between 1.0 and 1.0 × 105 Hz with an amplitude of 5 mV. EIS measurements were performed in 0.1 M KCl containing an equimolar mixture of $K_3[Fe(CN)_6]$ and $K_4[Fe(CN)_6]$ (total concentration: 2.5 mM).

2.4 Preparation of real samples

Paracetamol tablets (3 mg/tablet) were provided by a local pharmacy (Northeast Pharm, China). One tablet was completely pulverized in a mortar, and the powder was then collected. A defined amount of tablet powder was dissolved in deionized water to prepare a solution of APAP. The tap water was from the laboratory, and the urine samples were provided by the Department of Clinical Laboratory Medicine at The First Affiliated Hospital of Jinan University (Guangzhou, China). After diluting tap water and urine 10 times with deionized water, 0.1 M phosphate buffer was used to prepare APAP solutions at different concentrations, including 2, 4, 6, and 8 μM, using the standard addition procedure.

3. Results and discussion

3.1 Physical characterization

Transmission electron microscopy (TEM) was used to investigate the morphology of all samples. Flower-like MoS_2 and elongated CNTs are observed in Fig. 1a and b. Moreover, atomic force microscope images (Fig. S1) demonstrate that the average thickness of MoS_2 is 1.706 nm. The width of the MoS_2 nanosheets is approximately 200−250 nm, which is consistent with the TEM results. Fig. 1c shows that CNTs are well supported on the MoS_2 surface. The X-ray diffraction (XRD) patterns of samples containing CNTs are shown in Fig. 1d. The diffraction peaks of CNTs at around 26° and 42° match well with those of

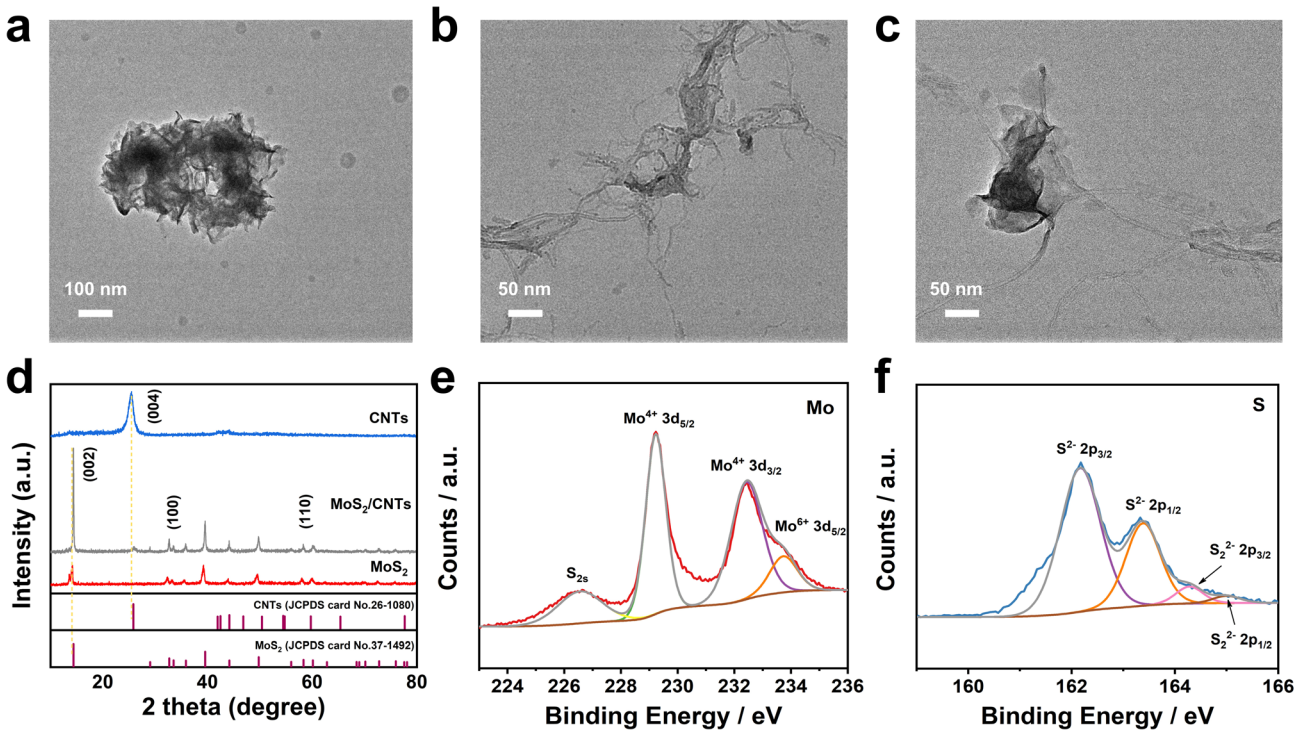

Fig. 1 TEM images (a–c) and XRD patterns (d) of MoS_2, CNTs and MoS_2/CNTs. XPS spectra of Mo 3d (e) and S 2p (f) for MoS_2.

the standard card (JCPDS card No. 26-1080),[28] corresponding to the planes of the hexagonal graphite-like structure. The XRD patterns of MoS_2 are consistent with its standard card (JCPDS card No. 37-1492), showing that CNTs were successfully loaded on the MoS_2 surface. The XRD patterns before and after the reaction (Fig. S2) show no noticeable changes, indicating that the crystalline structure of the MoS_2/CNTs composite remained stable throughout the reaction process. X-ray photoelectron spectroscopy (XPS) analysis confirmed the electronic states of the elements in MoS_2 (Fig. 1e and f). The $3d_{3/2}$ and $3d_{5/2}$ peaks of Mo are found at 232.5 and 229.1 eV, respectively, while the $2p_{1/2}$ and $2p_{3/2}$ peaks of S are observed around 163.3 and 162.1 eV, respectively.[29]

3.2 Electrochemical characterization

The electrochemical performance of every sensor was examined with the CV method in 0.1 M KCl solution containing 2.5 mM $K_3[Fe(CN)_6]/K_4[Fe(CN)_6]$. The results indicate that the MoS_2/CNTs sensor exhibits superior electrochemical performance, likely due to its high specific surface area and enhanced electrocatalytic activity, as illustrated in Fig. 2a.[30,31] Additionally, the Nyquist plots of the various sensors, presented in Fig. S3, reveal that the radius commonly used to denote charge transfer resistance was smallest for theMoS_2/CNTs sensor. This smaller radius suggests lower resistance, indicating superior conductivity,[32,33] which is consistent with the results of CV.

3.3 Electrochemical response to APAP of different sensors

As shown in Fig. 2b, three different modified electrodes, including MoS_2, CNTs, and MoS_2/CNTs electrodes, were used to detect APAP in 0.1 M phosphate buffer (pH 6.8) by the CV method. Notably, the MoS_2 sensor exhibited no redox peaks, which can be attributed to its low conductivity.[34] In contrast, a distinct redox peak was observed at 0.4 V for the MoS_2/CNTs electrode, surpassing those observed for the MoS_2 and CNTs alone. This implies that a synergistic effect was brought by the enormous specific surface area of MoS_2 and the effective electron transport capacities of CNTs. The enhanced electrical conductivity and specific surface area of the MoS_2/CNTs composite significantly facilitate electron transport during the oxidation of APAP. Fig. S4 shows the results of three measurements taken during the APAP detection process.

3.4 Optimization of detection conditions

The following four factors were chosen in order to establish the ideal parameters for APAP detection: (1) the optimal ratio (weight ratios of MoS_2 to CNTs were 3 : 1, 2 : 1, 1 : 1, 1 : 2 and 1 : 3), (2) the optimal pH, (3) the ideal deposition time, and (4) the ideal deposition potential. For each set of conditions, error-replicated tests were carried out. As shown in Fig. 2c and d, the optimal ratio and pH are 1 : 1 and 6.5, respectively. In Fig. 2d, the blue lines represent the linear correlation between pH and the corresponding peak, which can be displayed as $E_{pa} = (-0.0584 \pm 0.0019)\ pH + (0.8183 \pm 0.0132)$, $R^2 = 0.993$.

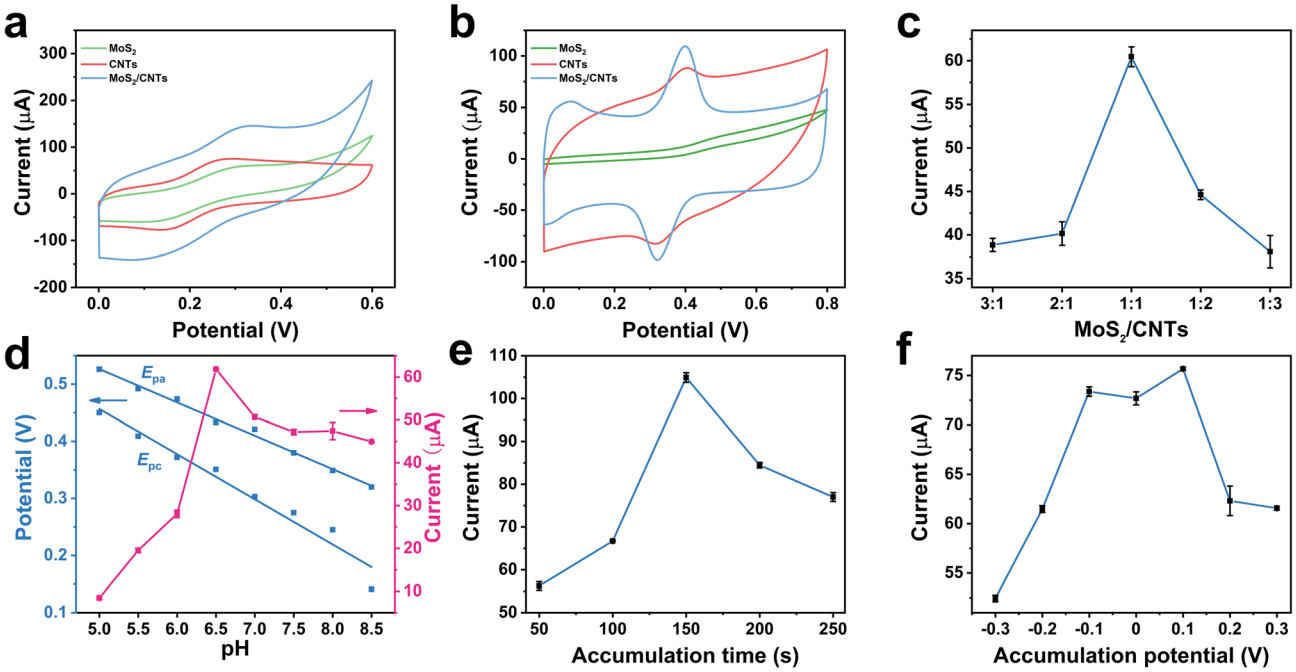

Fig. 2 CV curves (a) of MoS_2 (green curves), CNTs (red curves), and MoS_2/CNTs (blue curves) in a 2.5 mM $K_3[Fe(CN)_6]/K_4[Fe(CN)_6]$ solution containing 0.1 M KCl. CV curves (b) of different sensors in solutions containing 0.1 M phosphate buffer (pH = 6.8). Effect of different weight ratios of MoS_2/CNTs (c) on the peak current for 40 μM APAP in 0.1 M phosphate buffer (pH = 6.8). Effects of pH (d), accumulation time (e), and accumulation potential (f) on the peak current for 40 μM APAP in 0.1 M phosphate buffer (pH = 6.5) measured using MoS_2/CNTs sensor.

Additionally, the linear correlation between the pH value and reduction peak potential can be written as $E_{pc} = (-0.0791 \pm 0.0066)$ pH + (0.8521 ± 0.0450), $R^2 = 0.960$. Based on the formula $\frac{dE_P}{d\text{pH}} = 2.303 \frac{mRT}{nF}$, where m and n represent the number of protons and electrons, respectively. Ratios of m/n for the reduction and oxidation processes were calculated to be 0.33 and 0.99, respectively. The findings indicate that the exchange of protons is nearly equal to electrons in the stoichiometry of the APAP redox reaction.

Secondly, the accumulation process facilitates the electrochemical detection of APAP. The highest value for the oxidation current of APAP appeared when the accumulation potential was 0.1 V and the accumulation time was 150 s (Fig. 2e and f). Thus, 0.1 V and 150 s were chosen for all electrochemical measurements.

3.5 Effect of scan rate

A systematic investigation of the impact of scan rate on the electrochemical performance of the MoS_2/CNTs sensor was carried out. As shown in Fig. 3a, the redox peak current increases progressively with rising scan rates. Both the oxidation and reduction peak currents are proportional to the square root of the scan rate, as shown in Fig. 3b. The possible fitted regression equation is also presented. The electrochemical response to APAP by the MoS_2/CNTs sensor is governed by a diffusion-controlled mechanism, as evidenced by the linear correlation between the peak current and the square root of the scan rate.[35] The relationship between the redox peak potential and the logarithm of scan rates (log v) is illustrated in Fig. 3c. The oxidation peak potential gradually increases as log v increases, while the reduction peak potential gradually declines owing to the redox quasi-reversibility of APAP, in which the electron transfer rate is the same as the mass transport rate.

Based on the theory of Laviron,[36] the slope of the anodic line is equal to $2.3RT/(1-\alpha)nF$ and the slope of the cathodic line is equal to $-2.3RT/\alpha nF$ ($R = 8.314$, $T = 298$ and $F = 96\,480$). The constants α, n, R, and F represent the transfer coefficient, the number of electrons transferred in the reaction, the gas constant, and the Faraday constant, respectively. It was calculated that α was 0.58 and n was roughly 2.8, based on the slopes of the two straight lines according to the formula $E_{pa} = E^{0'} + \frac{2.3RT}{(1-\alpha)nF}\log v$ and $E_{pc} = E^{0'} - \frac{2.3RT}{\alpha nF}\log v$. The equation can be written as $\log \log \frac{k_a}{k_c} = \log \frac{\alpha}{1-\alpha}$ or $\frac{k_a}{k_c} = \frac{\alpha}{1-\alpha}$, while k_a is equivalent to the slope of $E_{pa}/\log v$ and k_c is equivalent to the slope of $E_{pc}/\log v$. Additionally, the following formula can be used to calculate the apparent heterogeneous electron rate transfer constant (k_s):[36]

$$\log k_s = \alpha \log(1-\alpha) + (1-\alpha)\log\alpha - \log\frac{RT}{nFv} - \frac{\alpha(1-\alpha)nF\Delta E_P}{2.3RT} \quad (1)$$

In this equation, n, ΔE_p, α and v represent the number of electrons involved in the process, the peak potential separation ($E_{pa} - E_{pc}$), the charge transfer coefficient and the scan rate, respectively. The number of transferred electrons can be estimated to be 2 as number of electrons is calculated as 2.8 in the reaction of APAP. Furthermore, the MoS_2/CNTs sensor exhibits an anodic peak at 0.399 V and a cathodic peak at 0.322 V,[20] which shows that the electrochemical reaction of APAP is a reversible process. This reversibility is further illustrated by the proposed mechanism depicted in Scheme 2. As shown,

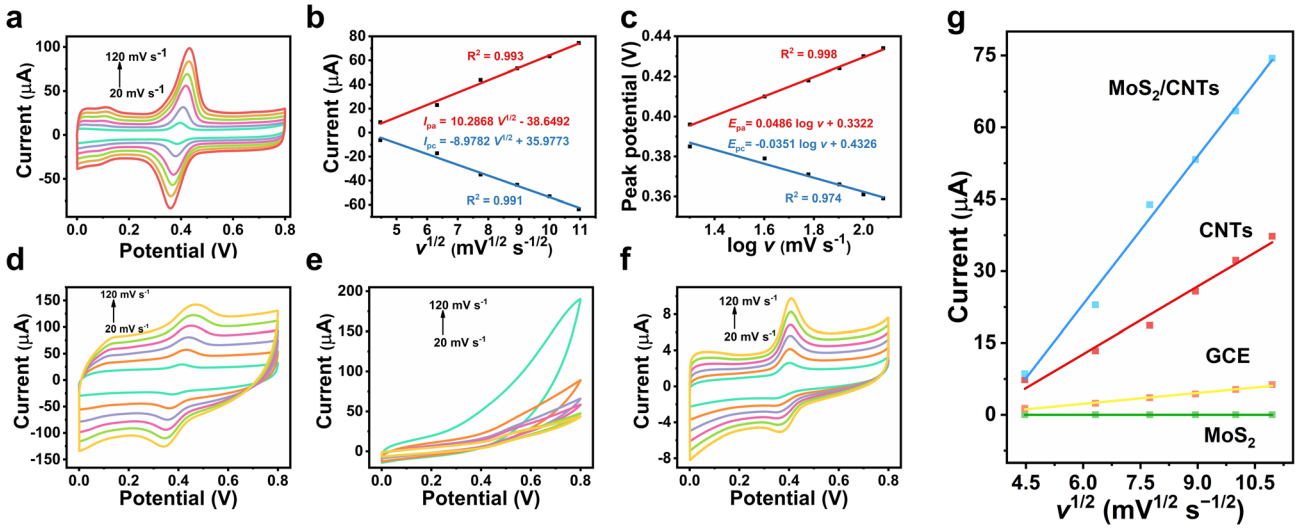

Fig. 3 (a) CV curves of MoS_2/CNTs/GCE in 0.1 M phosphate buffer (pH 6.5) with 40 μM APAP at different scan rates (from 20 to 120 mV s^{-1}). (b) Relationship between the redox peak currents of APAP and the square root of scan rates. (c) Dependence of the redox peak potentials of APAP on log v. CV responses of 40 μM APAP to different sensors in phosphate buffer (0.1 M, pH 6.5) at various scan rates. (d–f) Represent CV curves of the CNTs, MoS_2 and GCE sensors, respectively. Plots of peak current (I_{pa}) *vs.* square root of the scan rate ($mV^{1/2}$ $s^{-1/2}$) (g).

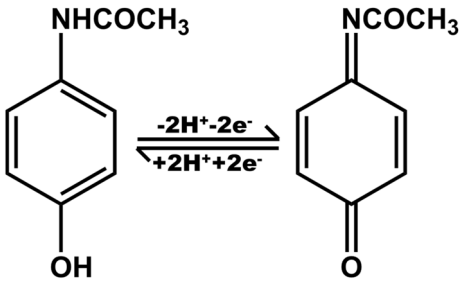

Scheme 2 Schematic of the electrochemical reactions of APAP.

reversible electron and proton transfer occur in APAP and *N*-acetyl-*p*-benzoquinonimine. Based on these findings, the potential detection mechanism of the MoS_2/CNTs sensor for APAP is represented in Scheme 3. While $v = 120$ mV s^{-1}, $\Delta E_p =$ 75 mV, and then $n\Delta E_p > 200$ mV. The k_s value for the oxidation reaction was calculated to be 0.932 s^{-1}, which is higher than those of previous reports.[37,38] The high k_s value demonstrates the effectiveness of the MoS_2/CNTs composite film in facilitating electron transfer between the solution and the electrode.

3.6 Electrochemically active surface area

Fig. 3d–f reveal that increasing the scan rate from 0.02 to 0.12 V s^{-1} leads to an increase in the oxidation peak current (I_{pa}) for various sensors. A linear relationship between the corresponding peak current and the square root of the scan rate is illustrated in Fig. 3g. The corresponding linear equations for the different sensors, including MoS_2/CNTs, CNTs, and GCE, can be expressed as $I = (10.2868 \pm 0.4394)\ v^{1/2}$ ($mV^{1/2}\ s^{-1/2}$) − (38.6492 ± 3.6765), $R^2 = 0.993$; $I = (4.7129 \pm 0.3205)\ v^{1/2}$ ($mV^{1/2}\ s^{-1/2}$) − (15.6216 ± 2.6812), $R^2 = 0.993$; $I = (0.7602 \pm 0.0377)\ v^{1/2}$ ($mV^{1/2}\ s^{-1/2}$) + (0.7602 ± 0.0377), $R^2 = 0.990$.

Compared to the GCE and MoS_2 sensors, the MoS_2/CNTs and CNT sensors likely exhibit larger specific surface areas and faster electron transport rates. The electrode effective surface area (ECSA) was estimated using the Randles–Sevcik equation, which can be stated as follows:

$$I_p = 2.69 \times 10^5 \times A \times D^{1/2} \times n^{3/2} \times C\ v^{1/2} \quad (2)$$

where n is the number of electrons participating in the reaction, v is the scan rate (V s^{-1}), A is the electrochemical surface area of the electrode (cm^2), D is the diffusion coefficient (6.20×10^{-6} $cm^2\ s^{-1}$),[32] C is the concentration of the molecule in the solution (mol cm^{-3}), and I_p is the peak current.

For APAP detection, the surface area was calculated from this equation, including $n = 2$ and the value of slope $= I_p/v^{1/2}$. Therefore, the effective surface area of GCE, CNTs, and MoS_2/CNTs can be calculated as 0.01 cm^2, 0.062 cm^2, and 0.136 cm^2, respectively. These values indicate thatMoS_2/CNTs has a larger ECSA, which is due to the efficient electron transport and abundant active sites of MoS_2/CNTs.

3.7 Performance of the MoS_2/CNTs sensor for APAP detection

Under the ideal conditions, the DPV method was used to detect varying concentrations of APAP with the MoS_2/CNTs sensor. As shown in Fig. 4a and b, the DPV curves, along with the corresponding linear fitting curves, are presented for APAP concentrations ranging from 0.07–10 μM and 10–150 μM, respectively. These linear relationships are described by the equations I_{pa} (μA) = (2.2292 ± 0.0326) C (μM) + (0.1621 ± 0.1208), $R^2 = 0.998$ (0.07–10 μM) (Fig. 4a) and I_{pa} (μA) = (0.3886 ± 0.0238) C (μM) + (21.8206 ± 2.9312), $R^2 = 0.985$ (10–150 μM) (Fig. 4b). The slope of the latter segment decreases significantly compared to that of

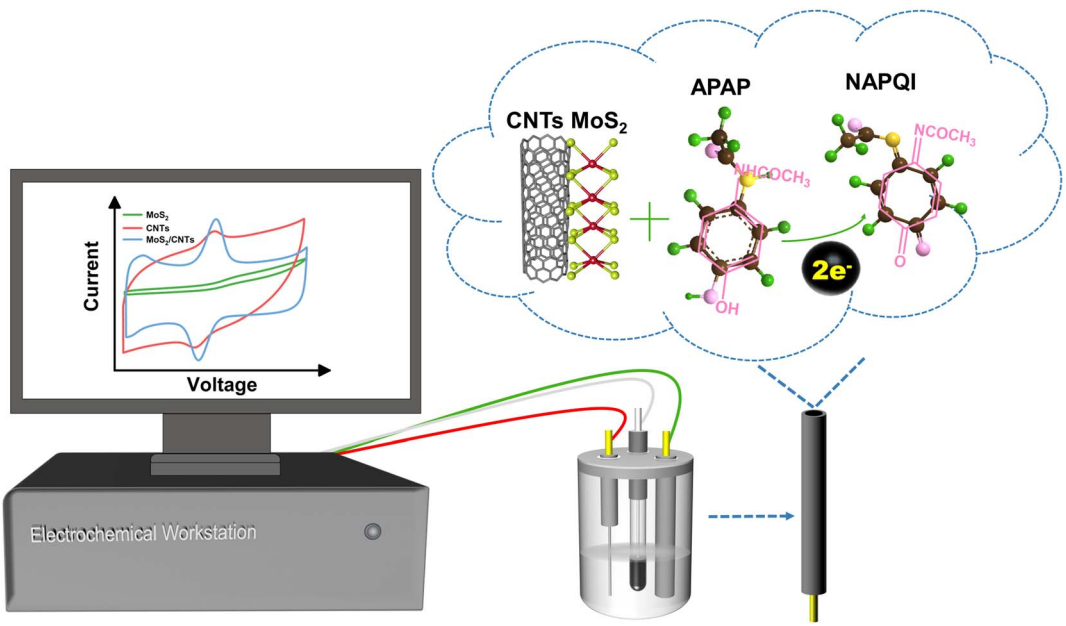

Scheme 3 Reaction mechanism for APAP detection by the MoS_2/CNTs sensor.

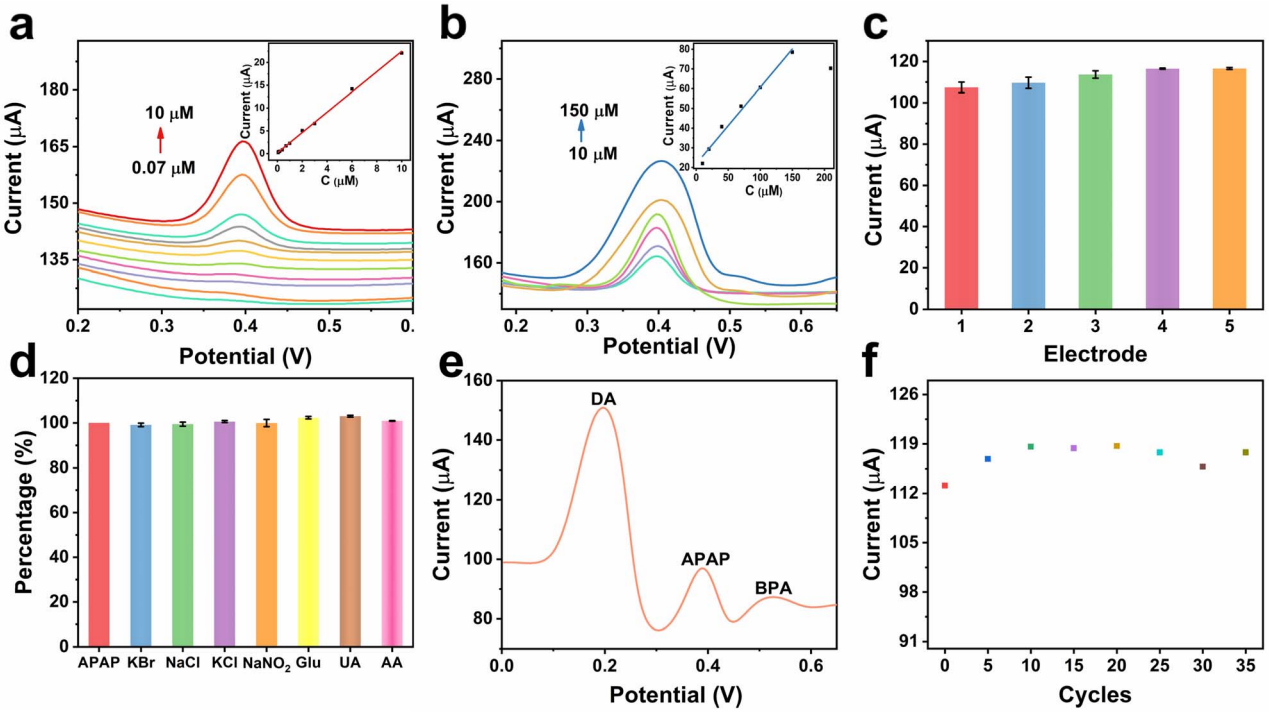

Fig. 4 (a) DPV curves of the MoS_2/CNTs sensor in 0.1 M phosphate buffer (pH 6.5) in the presence of 0.07–10 μM APAP. (b) DPV curves of the MoS_2/CNTs sensor in 0.1 M phosphate buffer (pH 6.5) in the presence of 10–150 μM APAP. Insets of (a) and (b) show the corresponding calibration curves. (c) Reproducibility, (d) interference effects, and (f) stability of the MoS_2/CNTs sensor for 40 μM APAP detection. DPV responses of the MoS_2/CNTs sensor for a mixture of BPA, APAP, and DA (e).

the earlier segment, which may be attributed to the saturation of electron dynamic behavior.[39] Once the concentration exceeds 150 μM, the peak current begins to decline, suggesting APAP saturation, as demonstrated by the fitted regression curve in Fig. 4b.[20] The LOD ($3S_b/S$) is calculated as 0.43 μM ($S_b = 0.320$), where S_b and S represent the standard deviation of the blank response and the sensitivity of the sensor or the slope of the calibration curve in the equation, respectively. As outlined in Table S1, the current sensor achieves a lower detection limit and a higher sensitivity value compared with the corresponding values reported in previous studies.

3.8 Reproducibility, stability and interference assessment

Reproducibility is a critical factor for electrochemical sensors. In this study, five MoS_2/CNTs electrodes were fabricated under identical conditions, and each completed five DPV experiments in a 0.1 M phosphate buffer (pH 6.5) with 40 μM APAP (Fig. 4c). The relative standard deviation (RSD) of the five electrodes was less than 2.8%, demonstrating the excellent repeatability of the composite electrode. As shown in Fig. 4d, interference was assessed by introducing various species such as KBr, NaCl, KCl, $NaNO_2$, glucose (Glu), uric acid (UA), and dopamine (DA) (each at 10 times the concentration of APAP) to monitor changes in

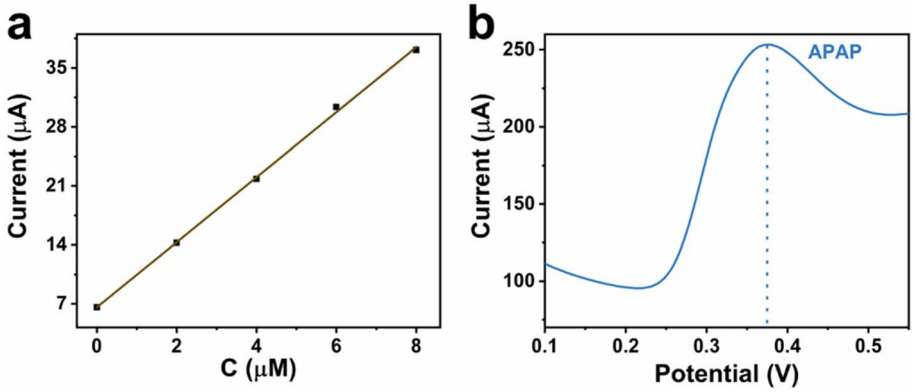

Fig. 5 Linear relationship between (a) peak current and different APAP concentrations in 0.1 M phosphate buffer (pH = 6.5) containing 0, 2, 4, 6, and 8 μM APAP. DPV signal (b) of a specified amount of an APAP tablet in 0.1 M phosphate buffer (pH = 6.5).

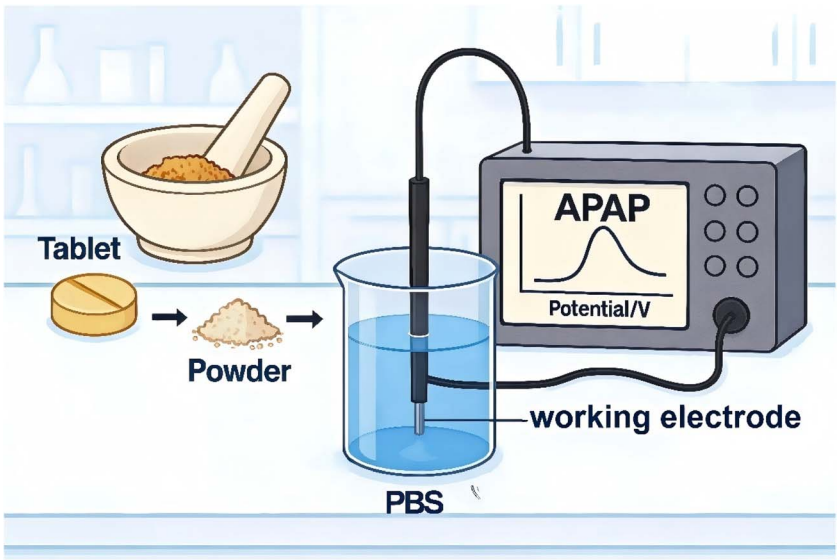

Scheme 4 Schematic of the setup used to detect APAP in real samples.

the oxidation peak current. The RSD values were all below 2% (Table S2). In order to further validate the system with respect to interference, 400 μM solutions of DA and BPA were added concurrently to 0.1 M phosphate buffer (pH 6.5) containing 40 μM APAP. The oxidation peak potentials of the three species were all separated, as displayed in Fig. 4e, indicating that this sensor has good anti-interference performance. The stability of the electrode was evaluated in a cycling repeatability experiment (Fig. 4f). The MoS_2/CNTs sensor maintained 104% of its initial peak current after 35 scans, which demonstrates that the electrode is stable.

3.9 Determination of APAP in real samples

To detect APAP in tap water, human urine, and tablets, the DPV method was applied. A human urine sample from a healthy volunteer without acetaminophen intake was used as a real matrix. A known amount of APAP standard was spiked into the sample to validate the applicability and recovery of the sensor, serving as a proof-of-concept test rather than a pharmacokinetic study. For APAP concentrations of 0, 2, 4, and 6 μM in 0.1 M phosphate buffer, the DPV signal and standard curve were expressed as: I_{pa} (μA) = (3.858 ± 0.0658) C_{BPA} (μM) + (6.6 ± 0.3222), $R^2 = 0.998$ (Fig. 5a). The standard addition method was applied to detect APAP by the DPV method. In addition, after adding a specified amount of powdered APAP tablet powder to 0.1 M phosphate buffer (pH 6.5), the DPV method was employed to detect APAP, thereby demonstrating that this sensor is feasible for practical applications (Fig. 5b). Excellent recovery rates between 90% and 110% were achieved by spiking various concentrations of APAP (2 μM, 4 μM, 6 μM, and 8 μM) into tap water and urine, with the recovery calculated using the standard curve equation. The application is shown schematically in Scheme 4. Moreover, the RSDs of the samples with various doses (Table S3) indicate that the sensor is effective for APAP detection in real samples. For comparison, real samples were also analyzed by HPLC (Table S4). The results confirmed that the proposed method can be used to detect APAP with the standard addition method.

4. Conclusion

For the purpose of detecting APAP, an electrochemical sensor based on a MoS_2/CNTs nanocomposite was effectively developed. The MoS_2 sheets were synthesized *via* a hydrothermal method, and the MoS_2/CNTs composite was created through simple physical mixing. The exceptional electrochemical surface area of MoS_2/CNTs provides ample active sites for the electrochemical oxidation of APAP, enhancing efficient electron transport. The sensor demonstrates a low LOD and excellent reproducibility, stability, and selectivity. Furthermore, it effectively detects APAP in real samples such as tap water and urine. This study highlights the potential MoS_2/CNTs sensors in drug detection, opening new opportunities in the field of electrochemical analysis.

Author contributions

Siying Fu: validation, investigation, writing – original draft. Juan Li: validation, investigation, writing – original draft. Kunru Liu: investigation, methodology. Huan Tao: investigation, methodology. Wenyan Guo: investigation, methodology. Qingbing Zha: writing – review & editing, supervision. Jinhua Li: writing – review & editing, supervision, Funding. Zhi Li: resources, writing – review & editing, supervision.

Conflicts of interest

The authors declare that they have no known competing financial interests or personal relationships that could have appeared to influence the work reported in this paper.

Data availability

The data supporting this article have been included as part of the manuscript and its supplementary information (SI). Supplementary information: additional experimental details and supporting data (2 texts, 4 tables and 4 figures). See DOI: https://doi.org/10.1039/d5ra07347b.

Acknowledgements

This work was supported by the Science and Technology Project of Guangzhou (2024A03J0809), the Science and Technology Project of Heyuan, China (Medical Technology Research and Development No. 010) and the Medical Scientific Research Foundation of Guangdong Province, China (B2023386).

References

1 Y. Ishitsuka, Y. Kondo and D. Kadowaki, *Biol. Pharm. Bull.*, 2020, **43**, 195–206.
2 R. E. Ferner, J. W. Dear and D. N. Bateman, *BMJ*, 2011, 342.
3 V. V. Kouznetsov, *RSC Adv.*, 2024, **14**, 9691–9715.
4 M. A. Munir, A. Inayatullah, S. Ibrahim, I. R. Rimba Putri, E. Emelda, A. Fatmawati and N. Nurhidayanti, *Int. J. Appl. Pharm.*, 2023, **15**, 195–205.
5 O. M. El-Abassy, M. G. Fawzy and E. B. Kamel, *Sci. Rep.*, 2025, **15**, 4119.
6 P. Soysa and S. Kolambage, *J. Natl. Sci. Found. Sri Lanka*, 2010, **38**, 131–137.
7 S. Emdadi, L. Sorouraddin Mh Fau - Denanny and L. Denanny, *Analyst*, 2021, **146**, 1326–1333.
8 X. Hou, H. Xu, T. Zhen and W. Wu, *Trends Food Sci. Technol.*, 2020, **105**, 76–92.
9 C. Zhu, G. Yang, H. Li, D. Du and Y. Lin, *Anal. Chem.*, 2015, **87**, 230–249.
10 M. Ramya, P. S. Kumar, G. Rangasamy, G. Rajesh, K. Nirmala, A. Saravanan and A. Krishnapandi, *Chemosphere*, 2022, **308**, 136416.
11 S. Ponnada, M. S. Kiai, S. Yadav, A. Palariya, C. S. R. Vusa, R. S. C. Bose, A. Nehra, S. Datta, R. Pawar and G. S. Martynkova, *Appl. Mater. Today*, 2024, **39**, 102310.
12 M. Chaudhary, A. Kumar, A. Devi, B. P. Singh, B. D. Malhotra, K. Singhal, S. Shukla, S. Ponnada, R. K. Sharma and C. A. Vega-Olivencia, *Mater. Adv.*, 2023, **4**, 432–457.
13 M. Wei, Y. Yuan, D. Chen, L. Pan, W. Tong and W. Lu, *Anal. Methods*, 2024, **16**, 6134–6155.
14 S. Y. Ahmed, P. Emerson, M. Selvaraj, W. Sultana and D. Bharathi, *Inorg. Chem. Commun.*, 2024, **164**, 112453.
15 S. Jeevitha, H. S. N. Prasad, M. B. Shivaswamy, M. S. Asha, S. R. Arjun, G. N. Chandana, M. A. Sangamesha, B. S. Madhukar, B. S. Hemanth and S. Thomas, *Ionics*, 2024, **30**, 8617–8630.
16 H. Lv, Z. Li, P. Yin, P. Wan and M. Zhu, *Chin. Chem. Lett.*, 2025, **36**, 110457.
17 M. N. Norizan, M. H. Moklis, S. Z. N. Demon, N. A. Halim, A. Samsuri, I. S. Mohamad, V. F. Knight and N. Abdullah, *RSC Adv.*, 2020, **10**, 43704–43732.
18 R. Subash, K. Madhivanan, R. Atchudan, S. Arya and A. K. Sundramoorthy, *Diam. Relat. Mater.*, 2025, **152**, 111940.
19 D. Balram, K.-Y. Lian, N. Sebastian and N. Rasana, *Appl. Surf. Sci.*, 2021, **559**, 149981.
20 A. U. Alam, Y. Qin, M. M. Howlader, N.-X. Hu and M. J. Deen, *Sens. Actuators, B*, 2018, **254**, 896–909.
21 Z. Li, S. Lan and M. Zhu, *Environ. Sci. Ecotechnol.*, 2024, **18**, 100329.
22 V. P. Kumar and D. K. Panda, *ECS J. Solid State Sci. Technol.*, 2022, **11**, 033012.
23 A. Patra, M. A. More, D. J. Late and C. S. Rout, *J. Mater. Chem. C*, 2021, **9**, 11059–11078.
24 Z. Wang, H. Li, Z. Liu, Z. Shi, J. Lu, K. Suenaga, S.-K. Joung, T. Okazaki, Z. Gu and J. Zhou, *J. Am. Chem. Soc.*, 2010, **132**, 13840–13847.
25 S. A. Getaneh, A. G. Temam, A. C. Nwanya, P. M. Ejikeme and F. I. Ezema, *Discov. Electrochem.*, 2025, **2**, 38.
26 S. Chetana, N. Kumar, P. Choudhary, G. Amulya, C. S. Anandakumar, K. G. B. Kumar and D. Rangappa, *Mater. Chem. Phys.*, 2023, **294**, 126869.
27 H. Zhang, J. He, C. Zhai and M. Zhu, *Chin. Chem. Lett.*, 2019, **30**, 2338–2342.
28 A. Nouralishahi, A. A. Khodadadi, Y. Mortazavi, A. Rashidi and M. Choolaei, *Electrochim. Acta*, 2014, **147**, 192–200.
29 S. Lan, C. Yu, E. Wu, M. Zhu and D. D. Dionysiou, *ACS Sustain. Chem. Eng.*, 2021, **2**, 101–109.
30 B. Liu, Z. Yi, Y. Yang, Y. Li, J. Yang and M. Zhu, *Appl. Catal., B*, 2023, **334**, 122788.
31 C. Zhai, M. Sun, L. Zeng, M. Xue, J. Pan, Y. Du and M. Zhu, *Appl. Catal., B*, 2019, **243**, 283–293.
32 Z. Li, H. Zhang, Q. Zha, C. Zhai, W. Li, L. Zeng and M. Zhu, *Microchim. Acta*, 2020, **187**, 1–9.
33 Y. C. Pan, Y. Wen, R. Zhang, Y. Y. Wang, Z. R. Zhang and H. F. Yang, *Appl. Surf. Sci.*, 2012, **258**, 3956–3961.
34 R. Sha and T. K. Bhattacharyya, *Electrochim. Acta*, 2020, **349**, 136370.
35 R. R. Pandey, H. S. Alshahrani, S. Krylyuk, E. H. Williams, A. V. Davydov and C. C. Chusuei, *Electroanal.*, 2018, **30**, 886–891.
36 E. Laviron, *J. Electroanal. Chem.*, 1979, **101**, 19–28.
37 M. Zheng, F. Gao, Q. Wang, X. Cai, S. Jiang, L. Huang and F. Gao, *Mater. Sci. Eng., C*, 2013, **33**, 1514–1520.
38 M. Houshmand, A. Jabbari, H. Heli, M. Hajjizadeh and A. Moosavi-Movahedi, *Solid-State Electron.*, 2008, **12**, 1117–1128.
39 E. Haghshenas, T. Madrakian and A. Afkhami, *Mater. Sci. Eng., C*, 2015, **57**, 205–214.